Metal hydride storage tanks real-time State of Charge estimation based on nonlinear observer with a non-observable subsystem

Mingrui Chen[a], Ramon Costa-Castelló[b,*], Carles Batlle[c] and Jing Na[d,e]

[a]Institut de Robòtica i Informàtica Industrial, CSIC-UPC. C/ Llorens i Artigas 4-6, 08028 Barcelona, Spain
[b]Escola Tècnica Superior d'Enginyeria Industrial de Barcelona (ETSEIB); Universitat Politècnica de Catalunya (UPC).
[c]Departament de Matemàtiques, Institut d'Organització i Control, EPSEVG, UPC, 08800 Vilanova i la Geltru, Spain
[d]Faculty of Mechanical and Electrical Engineering, Kunming University of Science and Technology, Kunming, 650500, PR China
[e]Yunnan Key Laboratory of Intelligent Control and Application, Kunming, 650500, PR China

ARTICLE INFO

Keywords:
Metal hydride tanks
Uncertain system dynamics estimator
State observer
State of Charge estimation

ABSTRACT

In this paper, a novel state of charge real-time estimation architecture for metal hydride storage tanks is proposed. Specifically, the state of charge estimation problem is converted into a nonlinear observer design problem. Firstly, the observability of the metal hydride tank model is analyzed and the state space is divided into three regions according to its observability. Secondly, an unknown system dynamic estimator is used to estimate the sorption rate of metal hydride tanks, which only requires information on tank pressure, temperature and flow rate. Thirdly, an observer is designed to estimate the density of hydrogen and metal hydride. Finally, the performance of the proposed estimator is validated using numerical simulation and experimental data.

1. Introduction

One approach to solving the intermittent and unstable characteristics of renewable energy is to produce hydrogen through electrolysis cells and store it using suitable technology [1]. The most common method of hydrogen storage is high-pressure compression. This well-developed technology provides high fill and release rates of hydrogen. However, the process of compressing hydrogen results in energy losses, and the calorific value of the compressed hydrogen is reduced by $13-18\%$, increasing overall operating costs [2]. In addition, the safety of compressed hydrogen transport is an issue that cannot be ignored. A safer technology is offered by liquefied hydrogen storage [3]. Since the pressure of liquid hydrogen storage is much lower, thinner and less costly tanks can be used [4]. The main shortages of liquefied hydrogen storage are the high cost of liquefying the hydrogen [5] and the boil-off phenomenon [6], which leads to large hydrogen leaks. Solid-state hydrogen storage, especially metal hydride (MH) hydrogen storage is a promising hydrogen storage technology. Compared to the other two methods, solid hydrogen storage technology is more suitable for long-term hydrogen storage owing to less leakage and the higher hydrogen density per unit volume of metal hydrides [7].

Metal hydride hydrogen storage tanks, as one of the carriers of solid hydrogen storage, have an important role in many applications, such as automotive applications [8]. To describe the dynamic behavior of the MH tanks, various models have been developed by researchers. These models can be classified as High-Fidelity Model (HFM)[9–14], Lumped parameter Model (LM) [15–19] and Hybrid Reduced Model (HRM) [20, 21]. HFMs take into account the distributed nature of the main variables used to describe system behavior. They are usually written using partial differential equations, and their main use is the design and analysis of system behavior. LM do not take into account the spatial variation of system variables, present low computational complexity, and are often used for the design of control systems and estimators. Finally, HRMs are a combination of models based on fundamental principles and experimental measurements, sometimes considering, in a simplified form, the distribution of certain variables. These allow for use in applications similar to LMs at a higher computational cost.

Gonzatti et al. [22] modeled a refrigerate MH large tank (diameter: 16.8cm; length: 125cm) assuming homogeneous temperature in the tank. Liu et al. [20, 21] proposed an HRM combining a state space model with data-driven methods. They also compared the performance of this approach with HFM simulations under conditions with temperature gradients, including the presence of fins inside the tank. The result shows that HRM can be applied to MH tanks with temperature gradients.

State of Charge (SOC) is one of the most important indicators for all energy storage devices including MH tanks. In the charging process, it is often desirable to reach a fully charged state without entering the overcharge region. It is not only about minimizing leakage, but it is also about safety. Therefore, it is necessary to monitor the SOC of MH tanks in real time for appropriate management. To estimate the SOC of MH tanks, the mass of hydrogen remaining in MH tanks needs to be calculated. In general, researchers usually use the integral of the flow rate to calculate the mass of hydrogen. Suárez et al. [23] calculated the mass of stored hydrogen m_{H_2} [kg] using the following equation:

$$m_{H_2} = m_{H_2}(0) + \frac{M_{H_2}}{22.4} \cdot \int_0^t \dot{m}_{H_2} dt \tag{1}$$

*Corresponding author
chenmingrui2018@gmail.com (M. Chen); ramon.costa@upc.edu (R. Costa-Castelló); carles.batlle@upc.edu (C. Batlle); najing25@163.com (J. Na)

where M_{H_2} [kg/mol] is the molar mass of hydrogen, 22.4 is the molar volume [m^3/mol] and $\dot{m}_{H_2}$ [m^3/s] is the volumetric flow rate.

The above equation requires the initial mass of hydrogen in MH tanks at the beginning of the measurement to be known, which is often difficult to assess accurately. In addition, using the integral to calculate the hydrogen mass introduces cumulative errors in the flow meter when the device operates for a long time, which causes large errors in the results. Zhu et al. [24] developed an empirical model based on Pressure-Composition-Temperature (PCT) curves and experimental data from which the SOC of MH tanks was estimated. However, since the method was developed based on PCT curves, it can only estimate the hydrogen mass of MH tanks under equilibrium conditions. Subsequently, they developed a joint state classifier to identify the current state of MH tanks and combined it with a previously developed empirical model to estimate the SOC of MH tanks online [25].

To the best of our knowledge, only a few results have been reported for SOC estimation of MH tanks, and the existing methods in the literature have more or less restrictions on the state of MH tanks when estimating the SOC, which is not able to meet the real-time monitoring of the SOC under most of the working conditions.

The objective of this work is to develop a state observer to estimate the SOC of MH tanks. State observers [26–30] are algorithms used to estimate the states of a given dynamic system. To do so they combine the dynamic system model and the input and output signals. Due to the strong nonlinearity of the MH tank model, we mainly focus on nonlinear observers. Unfortunately, unlike linear observers, there is no unified design method for nonlinear observers. Ciccarella et al. [31] extended the linear Luenberger observer to nonlinear uniformly observable systems, i.e. Luenberger-like observer, and a Kalman-like observer is proposed to extend the linear Kalman observer to nonlinear non-uniformly observable systems in [32]. These two methods are appropriate for systems having state-affine forms. For other forms, such as the triangular form, high-gain observers and high-gain Kalman observers are proposed. A Lipschitz triangular form is considered in [33] where the nonlinear Lipschitz constant is regarded as a disturbance in a high-gain observer, so the gain of the observer must be chosen large enough to compensate for this disturbance. Astolfi et al. [34] proposed low-power peaking-free high-gain observers to overcome the peaking phenomenon and limit the order of high-gain parameters by adding saturations at each block. For systems that do not satisfy the normal forms, the approach adopted by most researchers is to transform the original system into nominal form, then observe the state in normal form using existing observer structures and finally return the estimates to the original coordinates [35].

Differently from what it is required to compute (1), our observer does not need to know the value of $m_{H_2}(0)$. In addition, the designed SOC estimation method can run at time instant when MH tanks are working and does not require the SOC to be estimated only when MH tanks are in equilibrium, which is important for the thermal management of MH tanks.

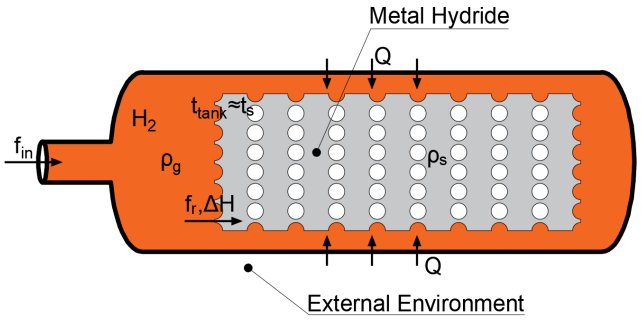

Fig. 1- Schematic of an MH tank (the process of charge) [36]. ρ_g and ρ_s are the density of hydrogen and MH. f_{in} and f_r are normalized mass flow rate and sorption mass flow rate of hydrogen. t_{tank} and t_s are the temperature of the tank and MH. Q is the heat exchange per unit volume from the ambient air to the MH tank and ΔH is the enthalpy change of the reaction.

Unlike (1), the method proposed in this work uses a combination of the data available through direct measurement and a mathematical model of the tank. The model used is relatively simple since it is basically a mass balance (the operating principles are similar in the different metal hydrides, so the model can be used with different types of metal hydrides). The model must be previously calibrated with the parameters of the metal hydride with which it is intended to work, this allows the algorithm to easily adapt to different types of metal hydrides. Therefore, the SOC estimation framework presented in this paper could be applicable to tanks with different metal hydrides.

The main contributions of this paper can be summarized as follows:

1. An unknown system dynamic estimator (USDE)-based estimator of the sorption rate of MH tanks is proposed, which makes it possible to monitor the sorption state of MH tanks in real time.
2. A nonlinear observer is proposed to estimate the SOC of the MH tank in real time.
3. The proposed estimator is validated using numerical and experimental data.

The paper is organized as follows: Section 2 describes the MH tank model tank and characterizes its observability. Section 3 describes the design of the sorption rate estimator and the nonlinear observers for MH tanks. In Section 4, simulations of the proposed nonlinear observer are provided and experimental results are given in Section 5. Finally, the conclusions are presented in Section 6.

2. MH tanks model and problem statement

2.1. Description of MH tanks

MH tanks are one of the container technologies most widely used for solid-state hydrogen storage. In general, MH

Nomenclature

Abbreviations

MH	Metal hydride
PCT	Pressure-Composition-Temperature
SOC	State of charge

Parameters

ρ_g	Density of hydrogen (kg/m^3)
m'_{in}	Mass rate of hydrogen (kg/s)
m'_r	Mass rate of hydrogen sorption (kg/s)
v_{tank}	Volume of tank (m^3)
v_{MH}	Volume of MH (m^3)
ε	Porosity of MH
f_{in}	Normalized mass flow rate of hydrogen (kg/m^3/s)
f_r	Normalized sorption mass flow rate of hydrogen (kg/m^3/s)
v_g	Normalized volume of hydrogen
ρ_s	Density of the MH (kg/m^3)
v_s	Normalized volume of the MH
c_a	Absorption constant (1/s)
c_d	Desorption constant (1/s)
E_a	Ectivation energy of absorption (J/mol)
E_d	Ectivation energy of desorption (J/mol)
$p_{eq,a}$	Equilibrium pressure of absorption (Pa)
$p_{eq,d}$	Equilibrium pressure of desorption (Pa)
R	Universal gas constant (8.314 J/mol/K)
ρ_{ss}	Saturated density of MH with complete absorption of hydrogen (kg/m^3)
ρ_{s0}	Empty density of the MH without any hydrogen (kg/m^3)
p	Pressure of hydrogen (Pa)
M_{H_2}	Molar mass of hydrogen (2.016×10^{-3} kg/mol)
v_{H_2}	Maximum volume of hydrogen that can be absorbed (m^3)
ρ_{H_2}	Density of hydrogen in standard state (kg/m^3)
p_0	Atmospheric pressure (101 325 Pa)
ΔS_d	Entropy change for desorption (J/mol/K)
ΔH_d	Enthalpy change for desorption (J/mol)
φ, φ_0	Plateau flatness coefficients
β	Plateau hysteresis coefficient
F_{in}	Flow rate of hydrogen (Ln/min)
p_{pipe}	Pressure of pipe (Pa)
k_p	Proportional coefficient
m_{total}	Maximum hydrogen capacity (kg)

Subscripts

a	Absorption
d	Desorption

tanks have a relatively simple structure, consisting mainly of internal metal alloys and a metal shell. The schematic of the MH tank is displayed in Fig. 1. During the charging process, hydrogen flows from the pipe into MH tanks at a certain normalized mass flow rate, f_{in}, and then reacts with the metal alloy to form the MH under a certain pressure. The process of discharging is the opposite. The main hydrogen storage alloys that have been validated to have high rates of hydrogen absorption and desorption include AB (TiFe), AB_2 ($TiMn_2$), AB_5 ($LaNi_5$), and A_2B (Mg_2Ni) [37, 38]. To increase the surface area of hydrogen in contact with the metal alloy and to accelerate the reaction rate, as shown in Fig. 1, the structure of the metal alloy is usually porous. The chemical equation of the absorption and desorption process is [7]

$$M + \frac{x}{2} H_2 \underset{\text{desorption}}{\overset{\text{absorption}}{\leftrightarrow}} MH_x + \Delta H, \tag{2}$$

where M is the metal alloy, MH_x is the MH and ΔH is the heat of reaction.

2.2. State-space model of MH tanks

As proposed in [39], the modeling of MH tanks includes dynamics of mass balance and thermal energy balance. To simplify the model, we assume that the temperature of MH tanks can be measured by thermocouples directly. Thus, it is not necessary to take the thermal energy balance into account in the model. The state-space form of MH tanks can be written as follows [40] (the modeling details are shown in Appendix A):

$$\dot{\mathbf{x}} = \mathbf{f}(\mathbf{x}, \mathbf{u}) = \begin{bmatrix} \dfrac{u_2 - f_r\left(x_2, u_1, y(x_1, u_1)\right)}{v_g} \\ \dfrac{f_r\left(x_2, u_1, y(x_1, u_1)\right)}{v_s} \end{bmatrix}, \tag{3}$$

$$y = h(\mathbf{x}, \mathbf{u}) = x_1 \frac{u_1 R}{M_{H_2}}, \tag{4}$$

where $\mathbf{x} \in \mathbb{R}^2$ is the state vector, $\mathbf{x} = [\rho_g, \rho_s]^{\mathrm{T}}$. $\mathbf{u} \in \mathbb{R}^2$ is the input vector, $\mathbf{u} = [t_{tank}, f_{in}]^{\mathrm{T}}$. $y \in \mathbb{R}$ is the output variable, i.e. the system pressure.

Despite the simplicity of the model, which does not take into account the distributed nature of tank behaviour, previous work have shown that this model is capable of adequately describing the evolution of the main variables of the system [39, 40].

2.3. Problem statement

2.3.1. Main objective

The main objective of this paper is to estimate the amount of hydrogen stored in the MH tank and further estimate the SOC of the MH tank. The MH tank SOC is defined as the percentage of the current hydrogen amount m_{H_2} to the maximum hydrogen capacity m_{total} of the MH tank [25]:

$$soc_{tank} \triangleq \frac{m_{H_2}}{m_{total}}. \tag{5}$$

Noting that $v_s\dot{x}_2 + v_g\dot{x}_1 = u_2$, m_{H_2} can be obtained as

$$\begin{aligned} m_{H_2} &= m_{H_2}(0) + v_{MH}\cdot\int_0^t u_2 dt \\ &= m_{H_2}(0) + v_{MH}\cdot v_s\cdot\big(x_2 - x_2(0)\big) \\ &+ v_{MH}\cdot v_g\cdot\big(x_1 - x_1(0)\big) \end{aligned} \tag{6}$$

where $m_{H_2}(0)$ is the initial hydrogen mass of the MH tank, $x_2(0)$ is the initial density of the MH and $x_1(0)$ is the initial density of the hydrogen. Note that $m_{H_2}(0) = v_{MH}\cdot v_s\cdot(x_2(0) - \rho_{s0}) + v_{MH}\cdot v_g\cdot x_1(0)$.

Although (6) can be used to obtain the soc_{tank}, all the initial conditions are required, and therefore this approach is not very convenient from a practical point of view. Alternatively, soc_{tank} can be computed as

$$soc_{tank} = \frac{v_{MH}v_g}{m_{total}}x_1 + \frac{v_{MH}v_s}{m_{total}}\left(x_2 - \rho_{s0}\right). \tag{7}$$

The value of x_1 can be obtained from measurable variables (i.e. temperature and pressure using (36)). Unfortunately, the value of x_2 can not be directly measured.

In order to obtain x_1 and x_2 simultaneously, a state observer [41] for system (3)-(4) is proposed. Before designing the observer, it is necessary to perform an observability analysis for (3)-(4), i.e. it is necessary to analyze if it is possible to reconstruct the state variable, $\mathbf{x}$ from the measured variables and the model. This problem is addressed in the following section.

2.3.2. Observability analysis

A state-space system is named instantaneous observable if different state trajectories $\mathbf{x}(t)$ do not generate the same output trajectory $y(t)$ [41, 42]. In other words, in our case, different state pairs (ρ_g, ρ_s) should correspond to different trajectories of tank pressure $p(t)$.

Instantaneous observability can be tested through the Jacobian matrix rank of the observability map [43]:

$$O_k(\mathbf{x}, \mathbf{u}, \dots, \mathbf{u}^{(k-2)}) = \begin{bmatrix} \mathbf{y} \\ \dot{\mathbf{y}} \\ \\ \vdots \\ \mathbf{y}^{(k-1)} \end{bmatrix}. \tag{8}$$

Table 1
Parameters of the MH tank model used in observability analysis [40]

Symbol	Value	Symbol	Value
ϵ	0.6992	v_{MH}	$0.353\times10^{-3}\,\mathrm{m}^3$
ρ_{s0}	$6350\,\mathrm{kg/m}^3$	ρ_{H_2}	$0.0897\,\mathrm{kg/m}^3$
R	$8.314\,\mathrm{J/(mol\cdot K)}$	p_0	101 325 Pa
M_{H_2}	$2.016\times10^{-3}\,\mathrm{kg/mol}$	v_{H_2}	$0.35\,\mathrm{m}^3$
v_{tank}	$0.48\times10^{-3}\,\mathrm{m}^3$	ΔS_d	$112.3193\,\mathrm{J/mol/K}$
ΔH_d	$2.6967\times10^4\,\mathrm{J/mol}$	φ	0.1770
φ_0	0.0030	β	0.2779
c_a	843.5713 1/s	c_d	3109.0 1/s
E_a	$3.2573\times10^4\,\mathrm{J/mol}$	E_d	$3.3151\times10^4\,\mathrm{J/mol}$

where $\mathbf{u}^k \triangleq \frac{d^k\mathbf{u}}{dt^k}$, $\mathbf{y}^k \triangleq \frac{d^k\mathbf{y}}{dt^k}$, where $k \in \mathbb{N}$, $k \geq n$ with n being the order of the state-space system. If

$$rank\left(\frac{\partial O_k}{\partial \mathbf{x}}\right) = n, \tag{9}$$

the system is locally instantaneous observable in $(\mathbf{x}, \mathbf{u}, \dots, \mathbf{u}^{(k-2)})$. Note that differently from what happens in linear systems the observability condition is a local property because it might depend on the state variable and the value of the input variable.

The observability map for (3)-(4), with $k = 2$, is:

$$O_2(\mathbf{x}, \mathbf{u}) = \begin{bmatrix} x_1\dfrac{u_1R}{M_{H_2}} \\ \dfrac{u_1R}{M_{H_2}}\cdot\dfrac{u_2 - f_r}{v_g} \end{bmatrix}. \tag{10}$$

Its Jacobian matrix takes the form

$$\frac{\partial O_2}{\partial \mathbf{x}} = \begin{bmatrix} \frac{u_1R}{M_{H_2}} & 0 \\ *_1 & *_2 \end{bmatrix}, \tag{11}$$

where[1]

$$*_1 = -\frac{u_1R}{M_{H_2}}\cdot\frac{\partial}{\partial x_1}\left(\frac{f_r\left(x_2, u_1, y(x_1, u_1)\right)}{v_g}\right), \tag{12}$$

$$*_2 = -\frac{u_1R}{M_{H_2}}\cdot\frac{\partial}{\partial x_2}\left(\frac{f_r\left(x_2, u_1, y(x_1, u_1)\right)}{v_g}\right). \tag{13}$$

To check if (11) is full rank, we compute its determinant:

$$\det\left(\frac{\partial O_2}{\partial \mathbf{x}}\right) = \frac{u_1R}{M_{H_2}}\cdot *_2\,. \tag{14}$$

If it is different from 0, O_2 will be full rank and consequently the system will be instantaneous observable.

As shown in (35), f_r is a piecewise-defined nonlinear function. The discussion about the rank of the Jacobian matrix $\frac{\partial O_2}{\partial \mathbf{x}}$ needs to be divided into two cases:

[1] It is assumed that u_2 does not algebraically depend on the state variables.

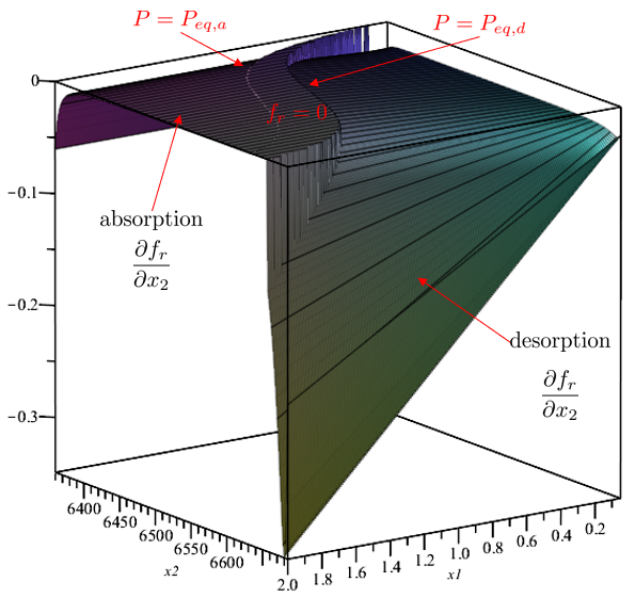

Fig. 2- Values of $\frac{\partial f_r}{\partial x_2}$ with a fixed $u_1 = 300\,\mathrm{K}$, $x_1 \in [0.05, 2]$ $(\mathrm{kg/m^3})$ and $x_2 \in [6360, 6685]$ $(\mathrm{kg/m^3})$ and the parameters shown in Table 1.

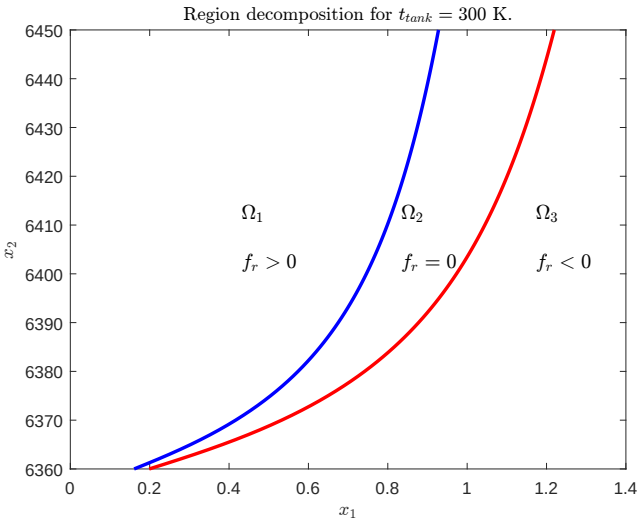

Fig. 3- Region decomposition for $u_1 = 300\,\mathrm{K}$, $x_1 \in [0.05, 2]$ $(\mathrm{kg/m^3})$ and $x_2 \in [6360, 6685]$ $(\mathrm{kg/m^3})$ and the parameters shown in Table 1.

1) Case 1: $f_r = 0$.
   In this case, f_r is a constant function, consequently, its partial derivatives will be zero, so $*_2$ and $\det\left(\frac{\partial O_2}{\partial \mathbf{x}}\right)$ will be identically zero and the system (3)-(4) will not be instantaneous observable. This means that it is not possible to construct an observer which reconstructs the system state from the model and the measurable variables.

   When $f_r = 0$, the tank pressure p is between the absorption equilibrium pressure $p_{eq,a}$ and the desorption equilibrium pressure $p_{eq,d}$ and there is no relationship between x_2 and the the measured variable, i.e. the pressure, p,.

2) Case 2: $f_r \neq 0$

   In this case, as u_1 is the Kelvin temperature of the MH tank, it will always be $u_1 > 0$ so the determinant will be different from 0 if $\frac{\partial f_r}{\partial x_2} \neq 0$. Therefore, checking the sign of the term $\frac{\partial f_r}{\partial x_2}$ is sufficient to determine the sign of $\det\left(\frac{\partial O_2}{\partial \mathbf{x}}\right)$.

   Analysing the expression of f_r, (35a), it can be found that terms $\ln\left(p/p_{eq,a}\right)$ and $(\rho_{ss} - \rho_s)$ are both monotonically decreasing with respect to ρ_s, so $\frac{\partial f_r}{\partial x_2}$ is monotonically decreasing in the absorption process. However, in the desorption process, (35b) shows that it is not monotone.

   f_r presents a fairly complex mathematical expression (it contains exponentials mixed with trigonometric functions). This makes it difficult to study it analytically, which is why a broad numerical analysis for $u_1 \in [275, 320]$ (K), $x_1 \in [0.05, 2]$ $(\mathrm{kg/m^3})$, $x_2 \in [6360, 6685]$ $(\mathrm{kg/m^3})$ and the parameters shown in Table 1 has been performed. This study has concluded that $\frac{\partial f_r}{\partial x_2} \neq 0$ and therefore the determinant will also be different from 0. As an example, Fig. 2 shows the evolution of $\frac{\partial f_r}{\partial x_2}$ for a temperature of 300 K. The middle region is the equilibrium region where $f_r = 0\,\mathrm{kg/m^3/s}$. It can be observed from Fig. 2 that $\frac{\partial f_r}{\partial x_2} \neq 0$ both in absorption and desorption region. The evolution of $\frac{\partial f_r}{\partial x_2}$ for other temperatures is very similar, and for the sake of space it is omitted here.

   With this study, it is concluded that the system (3)-(4) is instantaneous observable for $f_r \neq 0$.

   It should be noted that during the absorption and desorption processes the amount of hydrogen that passes from gas to solid or vice versa depends significantly on the value of x_1 and x_2, and therefore it is possible to establish a relationship between these variables, the model and the measured variables. It is during these processes that the state of charge can be estimated.

In summary, from the observability point of view, the space defined by the possible values of $[x_1, x_2]$ can be divided into the following three regions:

$$\begin{cases} \Omega_1 : \left\{[\mathbf{x}, \mathbf{u}] \mid p > p_{eq,a}\right\}, & \text{observable} \\ \Omega_2 : \left\{[\mathbf{x}, \mathbf{u}] \mid p_{eq,d} \leq p \leq p_{eq,a}\right\}, & \text{non-observable} \\ \Omega_3 : \left\{[\mathbf{x}, \mathbf{u}] \mid p < p_{eq,d}\right\}. & \text{observable} \end{cases}$$

Fig. 3 shows the space decomposition for $u_1 = 300$K. Note that the region definition can also be equivalently described

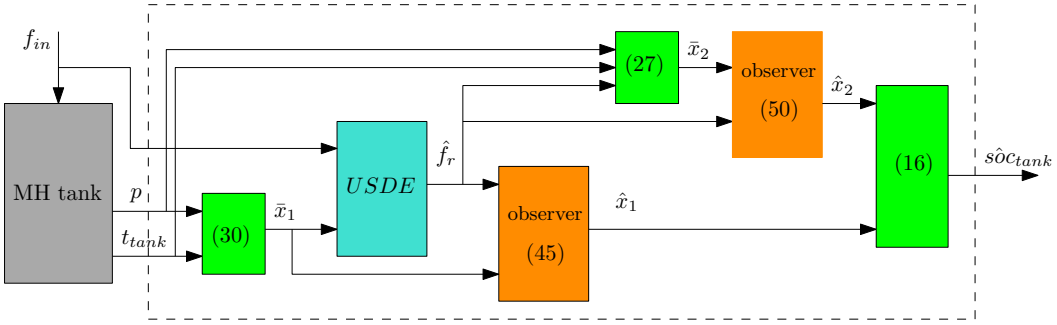

Fig. 4- Components of the proposed MH tank SOC estimation architecture.

in terms of f_r as follows:

$$\begin{cases} \Omega_1 : \{[\mathbf{x},\mathbf{u}] \mid f_r > 0\}, & \text{observable} \\ \Omega_2 : \{[\mathbf{x},\mathbf{u}] \mid f_r = 0\}, & \text{non-observable} \\ \Omega_3 : \{[\mathbf{x},\mathbf{u}] \mid f_r < 0\}, & \text{observable} \end{cases} \tag{15}$$

Remark 1. It should be noted that the concept of observability that we analyze here is for the complete system, i.e., whether it is possible to reconstruct unique pairs of states based on the output trajectory. For the case $f_r = 0$, although the complete system is non-observable, fortunately, since the output trajectory contains only information about measurable u_1 and x_1, x_1 and y are one-to-one, i.e., the mapping $x_1 \in X_1 \to y \in Y$ is bijective, making it possible to recover the system state x_1 through y. Thus, x_1 can be recovered from y in the whole state space. In contrast, there is no one-to-one correspondence between x_2 and y in the case $f_r = 0$. Considering the two different properties of the system state, we design observers for x_1 and x_2 separately in the following section.

Remark 2. Although the observability analysis in this paper uses specific model parameters, we would like to emphasise that this observability analysis is also applicable to other cases with different model parameters and, therefore, to MH tanks with different MH materials. The difference is only in the model parameters.

3. SOC estimation architecture

3.1. Main idea

In the literature, there are no techniques that allow directly designing observers for systems that present non-observable regions and a hybrid structure (it should be noted that f_r is piecewise defined). For this reason, an ad-hoc structure has had to be thought of that allows estimating the states of the system taking into account what region of space it is in.

As noticed, a variable of great relevance in the proposed MH tank model, see Section 2.2, is f_r. From it, it is possible to determine what region of space the system is in and calculate a large part of the dynamics of the system. Therefore, the first thing that has been done is to develop an estimator of the value of f_r, $\hat{f}_r$. A USDE is used for this purpose. Its development is presented in Section 3.2.

Once $\hat{f}_r$ is obtained and taking advantage of the fact that x_1 is always observable, a Luenberguer-like observer for x_1 will be developed. This observer will use the estimation of $\hat{f}_r$ and equation (4). The combination of these two elements will provide a more robust and smooth estimation, $\hat{x}_1$. The development and analysis of this Luenberguer-like observer is discussed in Section 3.3.

Finally, an observer for x_2 will be developed. x_2 is a variable that is not always observable, consequently, the value of the estimation of x_2, $\hat{x}_2$, will not always be active. It can only update its value when the system is in the observable regions.

Looking at equation (3) it can be seen that the derivative of x_2 can be estimated from $\hat{f}_r$. Unfortunately, $\hat{f}_r$ by itself cannot provide information about the value of x_2. The only way to obtain this information is using equation (35).

In regions Ω_1 and Ω_3, (35) is a C^1 function with nonzero derivatives with respect to x_2 (with u_1 and y fixed), thus, based on inverse function theorem, there exists functions $x_2 = \psi_1(f_r, u_1, y)$ and $x_2 = \psi_2(f_r, u_1, y)$ defined in Ω_1 and Ω_3 respectively. Consequently, ψ_1 and ψ_2 can be used to obtain the value of x_2 when the system is in an observable region. Let us define $\bar{x}_2$ as follows

$$\bar{x}_2 = \begin{cases} \psi_1(\hat{f}_r, u_1, y), & x_2 \in \Omega_1 \\ \text{not defined}, & x_2 \in \Omega_2 \\ \psi_2(\hat{f}_r, u_1, y). & x_2 \in \Omega_3 \end{cases} \tag{16}$$

Finally, combining $\bar{x}_2$ and $\hat{f}_r$, a Luenberguer-like observer will be developed. This observer will allow us to obtain $\hat{x}_2$. The convergence of this last observer will only be guaranteed if the system spends enough time in the observable regions. The development and analysis of this observer will be presented in Section 3.4.

Fig. 4 shows a graphical scheme of the complete observer architecture. The diagram shows how the different variables and estimators interact with the other. As will be

shown later, if the right conditions are satisfied, the proposed observer will be able to estimate all the state variables and from them the MH tank state of charge.

3.2. Estimator for sorption rate f_r

To estimate the sorption rate of MH tanks, we mainly use

$$\dot{x}_1 = \frac{u_2 - f_r}{v_g}. \tag{17}$$

From this equation, it is possible to compute

$$f_r = u_2 - v_g \dot{x}_1 \tag{18}$$

Since $y = p$ is a measurable variable, $x_1 = \rho_g$ can be calculated from (36) as

$$\bar{x}_1 \triangleq \frac{y \cdot M_{H_2}}{R \cdot u_1}. \tag{19}$$

In view of the fact that u_2 is a measured variable, it is possible to estimate f_r by combining (18) with (19). Unfortunately, this would imply differentiating (19). The derivative is a complex operation and very sensitive to measurement noise. To avoid this derivative, a USDE is proposed.

Before designing the USDE, the following assumption is needed [44].

Assumption 1. *The normalized sorption mass flow rate f_r and its derivative are bounded, and we assume that $\sup_{t\geq 0}|\dot{f}_r| \leq \lambda$ for a positive constant $\lambda > 0$.*

Remark 3. Assumption 1 is reasonable in the practical MH tank system described by (35). From the manual of MH tanks, it is known that the tank has maximum and minimum operating temperatures, so terms $c_a e^{-E_a/RT}$ and $c_d e^{-E_d/RT}$ in (35) are both bounded. Besides, the existence of the limiting operating pressure of MH tanks bounds the density of the MH, ρ_s, between empty density ρ_{s0} and saturated density ρ_{ss}. Thus equilibrium pressures, $p_{eq,a}$ and $p_{eq,d}$, are both bounded.

We first describe the filter operation $(\cdot)_f = [\cdot]/(\kappa s + 1)$ for known variables $\bar{x}_1$ and measured u_2:

$$\begin{cases} \kappa \dot{u}_{2f} + u_{2f} = u_2, & u_{2f}(0) = 0 \\ \kappa \dot{x}_{1f} + x_{1f} = \bar{x}_1, & x_{1f}(0) = 0 \end{cases} \tag{20}$$

where κ is the tunable parameter of the low-pass filter, u_{2f} and x_{1f} are the filtered variables of u_2 and $\bar{x}_1$, respectively. Then the following lemma is satisfied.

Lemma 1. *For the subsystem (17) and filter operation (20), there exists an exponentially convergent invariant manifold $\mathcal{M}_{x_1} = 0$ such that*

$$\lim_{\kappa\to 0}\left[\lim_{t\to\infty} \mathcal{M}_{x_1}\right] = 0, \tag{21}$$

holds for any $\kappa > 0$. Manifold variable $\mathcal{M}_{x_1}$ is defined as

$$\mathcal{M}_{x_1} = v_g \cdot \frac{\bar{x}_1 - x_{1f}}{\kappa} + f_r - u_{2f}. \tag{22}$$

PROOF. See Appendix B.

As shown in Lemma 1, especially (22), the normalized sorption mass flow rate f_r has a mapping relationship with the known variable x_1, filtered variables x_{1f} and u_{2f}. Then utilizing the property of the invariant manifold, we can design an estimator for the normalized sorption mass flow rate f_r:

$$\hat{f}_r = u_{2f} - v_g \cdot \frac{\bar{x}_1 - x_{1f}}{\kappa}. \tag{23}$$

Theorem 2. *For the subsystem (17) with estimator (23), the estimation error of the normalized sorption mass flow rate $\tilde{f}_r = f_r - \hat{f}_r$ exponentially converges to $\kappa\lambda$ as time goes to infinity.*

PROOF. See Appendix C.

Remark 4. As shown in the analysis provided in the Appendix C, $\hat{f}_r$, and thus the estimated signal of the estimator we designed is the low-pass filtered version of the true normalized sorption mass flow rate f_r. Therefore, a phase delay between the estimation and the true value is unavoidable. The phase delay can be reduced by decreasing the filter coefficient κ. However, a small κ would reduce the robustness of the estimator, so a suitable κ needs to be chosen for the practical scenarios.

3.3. Observer for hydrogen density ρ_g

In order to estimate x_1, a Luenberguer-like observer is proposed. The observer uses (17) as the model, and the value of x_1 obtained from (19) for the feedback term. Taking this into account the following observer is proposed:

$$\dot{\hat{x}}_1 = \frac{u_2 - \hat{f}_r}{v_g} + l_1 \cdot \left(\bar{x}_1 - \hat{x}_1\right), \tag{24}$$

where l_1 is a tunable constant observer gain and $\hat{f}_r$ is the signal generated by estimator (23). Then, the following theorem can be proved.

Theorem 3. *For the subsystem (17) with estimator (23) and observer (24), the observer error $\tilde{x}_1 = \bar{x}_1 - \hat{x}_1$ exponentially converges to $\kappa\lambda/(l_1 v_g)$ as time goes to infinity.*

PROOF. See Appendix D.

3.4. Observer for metal hydride density ρ_s

Considering the following subsystem

$$\dot{x}_2 = \frac{f_r}{v_s}. \tag{25}$$

a Luenberger-like observer will be proposed. As it has been analysed in Section 2.3.2, the system (3)-(4) is not always observable. In particular, it is the subsystem corresponding to (25) the one that loses observability when $f_r = 0$. In the non-observable regions, the observer feedback terms can

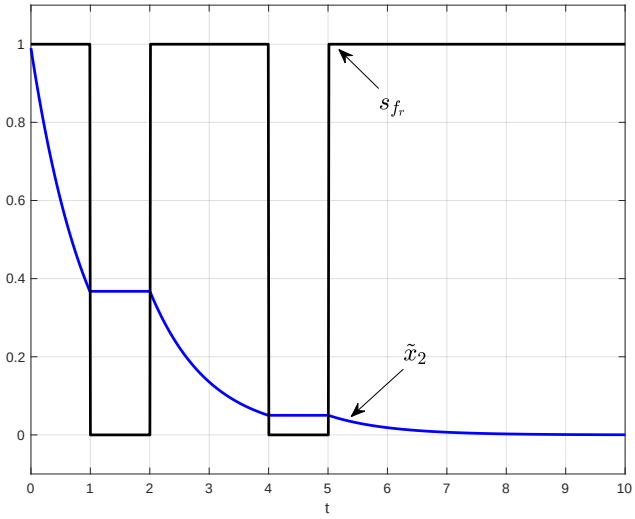

Fig. 5- Evolution of the estimation error, (29), for $l_2 = 1$, $\tilde{f}_r = 0$ and $\tilde{x}_2(0) = 1$.

not be used because there is no relationship between the measured variables and x_2. Taking this into account the following observer is proposed:

$$\dot{\hat{x}}_2 = \frac{\hat{f}_r}{v_s} + s_{f_r} \cdot l_2 \cdot \left(\bar{x}_2 - \hat{x}_2\right), \tag{26}$$

where l_2 is a tunable constant observer gain, $\bar{x}_2$ is the value of x_2 obtained from (16), and s_{f_r} is the time-varying switching function:

$$s_{f_r}(t) = \begin{cases} 1, & |\hat{f}_r| > \mu \\ 0, & |\hat{f}_r| < \mu, \end{cases} \tag{27}$$

where $\mu > 0$ is the tunable tolerance of $\hat{f}_r$.

Based on the observable region decomposition introduced in (15), $s_{f_r}(t)$ indicates if the system is in an observable region or not, i.e. x_2 is observable or not. As f_r is not directly available, this classification is made based on $\hat{f}_r$. Since $\hat{f}_r$ has an exponential convergence and it is the result of a numerical computation it will never be exactly equal to 0. Therefore, when $|\hat{f}_r| < \mu$, where μ is a small constant to be defined, we consider the system has entered the non-observable region.

Note that the feedback term of the Luenberger-like observer (26) turns off when the system is in a non-observable region.

Let us define the observer error as $\tilde{x}_2 \triangleq x_2 - \hat{x}_2$. Under the assumption that $\bar{x}_2 = x_2$, the observer error derivative is given by:

$$\begin{aligned} \dot{\tilde{x}}_2 &= \dot{x}_2 - \dot{\hat{x}}_2 = -s_{f_r} l_2 \tilde{x}_2 + \frac{1}{v_s} \cdot (f_r - \hat{f}_r) \\ &= -s_{f_r} l_2 \tilde{x}_2 + \frac{\tilde{f}_r}{v_s}, \end{aligned} \tag{28}$$

Table 2
Thermodynamic model and rest parameters [40].

Symbol	Value	Symbol	Value
ΔH_a	2.072×10^4 J/mol	T_{amb}	298.15 K
C_{pg}	14 890 J/(kg · K)	C_{ps}	6255.4 J/(kg · K)
k_{amb}	0.7485 J/(s · K)	ρ_{si}	6363.7 kg/m^3
k_p	0.8487	m_{total}	0.0315 kg

with solution of (28) is

$$\tilde{x}_2(t) = \phi(t) \cdot \tilde{x}_2(0) + \phi(t) \cdot \int_0^t \frac{\tilde{f}_r(\tau)}{v_s} \phi(\tau) d\tau, \tag{29}$$

where $\phi(t) = e^{-l_2 \int_0^t s_{f_r}(v) dv}$.

Fig. 5 shows the evolution of the estimation error, (29), for $l_2 = 1$, $\tilde{f}_r = 0$, $\tilde{x}_2(0) = 1$ and a given profile s_{f_r}. As it can be seen when $s_{f_r} = 1$, i.e. the system is in an observable region, the estimation error is exponentially reduced. On the contrary, when $s_{f_r} = 0$, i.e. the system is in a non-observable region, the estimation error is frozen and there is no convergence. Therefore, if the system is in an observable region for a sufficient amount of time, the estimation error would be sufficiently small. It is worth mentioning that the required time can be adjusted by appropriately selecting the value of l_2.

In order to establish some facts about the estimation error obtained, a hypothesis will be made about the percentage of time that the system is in an observable region. Let us define t_{obs} as the amount of time such that $s_{f_r} = 1$, i.e. the system is in an observable region, in the interval of time $[0, t]$. Then the ratio of time, ϖ, that the system is in an observable region can be defined as

$$\varpi \triangleq \frac{t_{obs}}{t}. \tag{30}$$

Assumption 2. *Absorption or desorption exists during the operation of MH tanks, i.e.* $\varpi \neq 0$.

Theorem 4. *Under the Asssumption 2, observer* (26) *makes the estimation error,* $\tilde{x}_2$*, exponentially converge to a ball of radius* $\frac{\|\tilde{f}_r\|_\infty}{(v_s \cdot l_2 \cdot \varpi)}$ *as time goes to infinity. In other words:*

$$\lim_{t \to \infty} |\tilde{x}_2| < \frac{\|\tilde{f}_r\|_\infty}{l_2 \varpi}$$

PROOF. See Appendix E.

Remark 5. ϖ is not a tunable parameter and it depends on the operation condition of MH tanks. Therefore, the bound of the observer error $\tilde{x}_2$ depends not only on the tunable gain l_2, but also on the value of ϖ. When $\varpi = 1$, the observation error $\tilde{x}_2$ exponentially converges to a ball of radius $\frac{\|\tilde{f}_r\|_\infty}{(v_s \cdot l_2)}$.

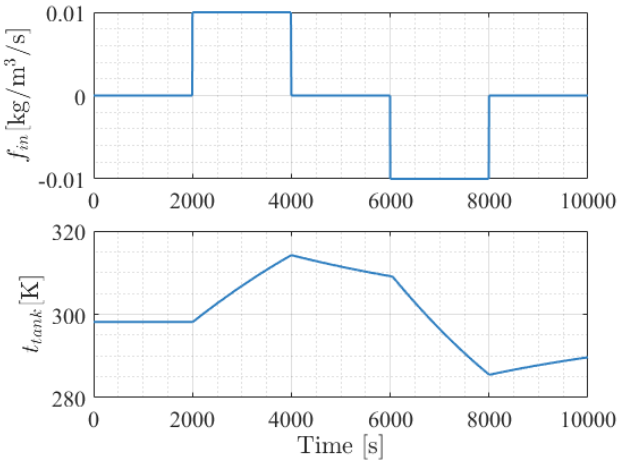

Fig. 6- Evolution of f_{in} and t_{tank} for the system (3) in the simulation Case I.

4. Numerical simulations

In this section, the viability of the proposed observation scheme is validated through two numerical simulations. Since one of the main difficulties encountered during the design of the algorithm is the transition between the different observability regions, two cases have been designed, which despite not occurring frequently during practical application, allow checking the behavior of the observer during these transitions.

In the first simulation, the initial state of the MH tank is in equilibrium (Case I) while in the second simulation is in the absorption phase (Case II). The temperature evolution is generated by the thermodynamic model of MH tanks. More specific details can be found in (27) and (28) of [40]. Parameters in Table 1 are used and the rest of the parameters used in simulations are listed in Table 2.

As stated in the previous section, the approximation of x_2, $\bar{x}_2$ is needed in observer (26). In these simulations, $\bar{x}_2$ is obtained by numerical computing (16), i.e. (35) is numerically inverted, at each time.

4.1. Case I

In the first case, we assume that the initial condition of the MH tank is in equilibrium. The normalized mass flow rate, f_{in}, has the profile shown in Fig. 6. Initial value of temperature is $t_{tank}(0) = 298.15\,\mathrm{K}$. The evolution of the temperature can also be seen in Fig. 6.

The observer parameters have been selected as $\kappa = 0.1$, $\mu = 1e-3$, $l_1 = 20$ and $l_2 = 0.1$. The value of κ should be chosen appropriately to balance the robustness and the convergence speed based on Remark 4. As the estimation of x_1 and x_2 depend directly on the estimation of $\hat{f}_r$, μ has been selected so that the convergence of $\hat{f}_r$ is faster than the other two. In the case of x_1 and x_2, the observer offers a balance between what is predicted by the model and the estimation of the variables $\bar{x}_1$ and $\bar{x}_2$. Since the estimation of x_1 is simpler and more direct, a faster convergence time has been selected than that of x_2.

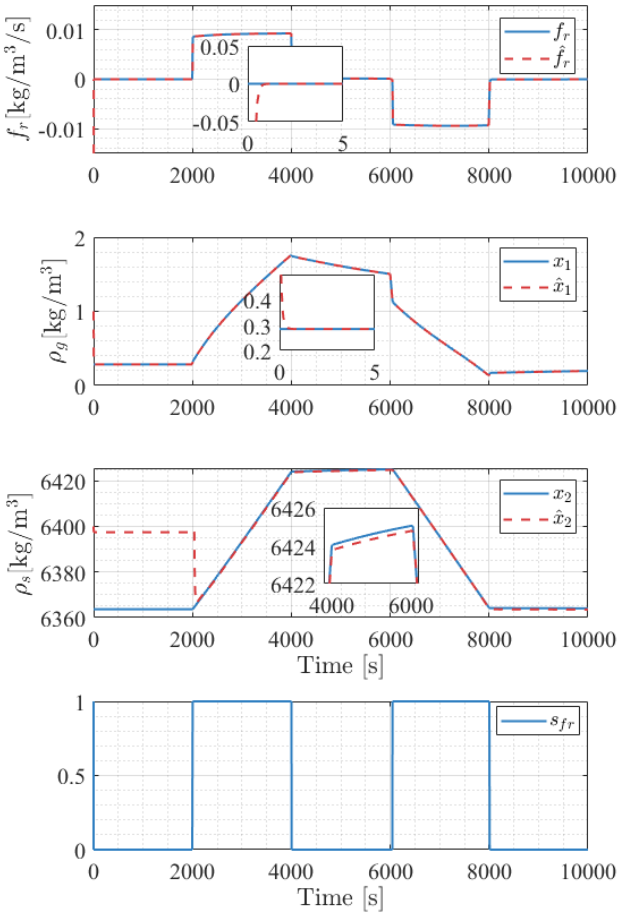

Fig. 7- Comparison of estimator and observer results with true values for the simulation in Case I.

The system initial conditions are taken as $x_1(0) = 0.3253\,\mathrm{kg/m^3}$, $x_2(0) = 6363.7\,\mathrm{kg/m^3}$, and the observer initial conditions are taken as $\hat{x}_1(0) = 1\,\mathrm{kg/m^3}$, $\hat{x}_2(0) = 6400\,\mathrm{kg/m^3}$.

The results of the simulation are illustrated in Fig. 7. It can be noticed that the sorption rate estimator $\hat{f}_r$ and the density of hydrogen $\hat{x}_1$ converge quickly to the bounded area within the first 5s and then perform well after that time. The convergence time and boundness can be adjusted by the tuning parameter in (23) and (24).

From the figure of $\hat{x}_2$, it can be found that $\hat{x}_2$ does not converge at $t \in [0, 2000s)$ since the first stage is in the non-observable region.

It is also worth noting that $\hat{x}_2$ changes at the beginning despite the true value of f_r being 0, the reason is that $\hat{f}_r$ needs some time to converge to the true value.

After 2000s, the trajectories of states enter the observable region and $s_{fr} = 1$, thus $\hat{x}_2$ converges gradually. Then, after 4000s, the trajectories of states enter the non-observable region again and $s_{fr} = 0$, so $\hat{x}_2$ gradually deviates from the true value. The observer $\hat{x}_2$ converges fast after 6000s and then gradually deviates from the true value

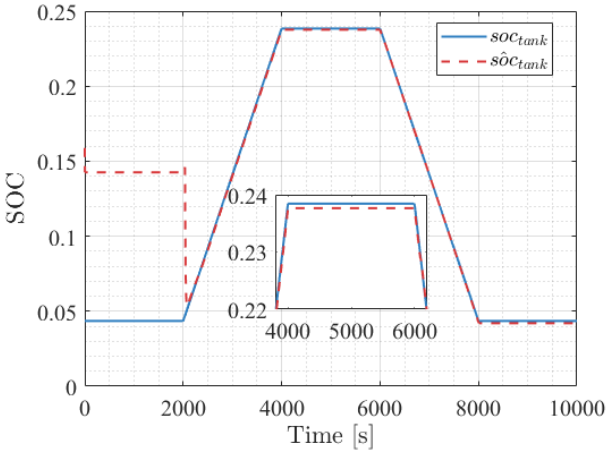

Fig. 8- Comparison of SOC estimation with true values for the simulation in Case I.

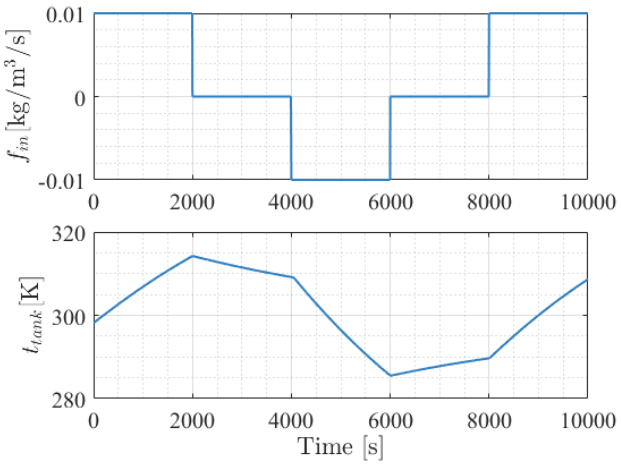

Fig. 9- Evolution of f_{in} and t_{tank} for the system (3) in the simulation Case II.

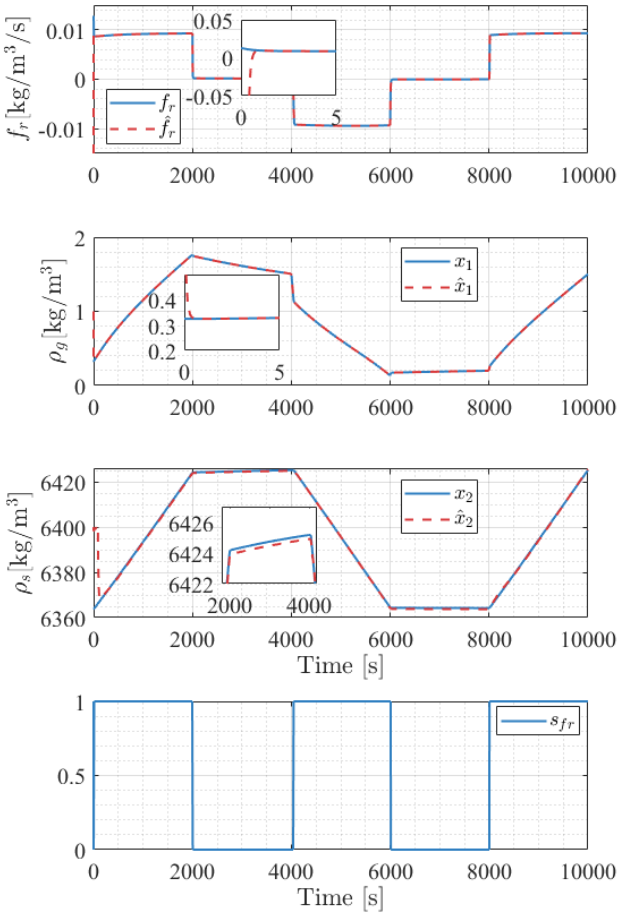

Fig. 10- Comparison of estimator and observer results with true values for the simulation in Case II.

after 8000s. The switching between observable and non-observable regions can be seen from the figure of s_{fr}.

The SOC estimation of MH tanks $\hat{soc}_{tank}$ is shown in Fig. 8.

It is shown that the estimation of SOC has the same trend as the estimation of x_2, i.e., the proposed SOC estimation framework can accurately estimate the value of SOC in the observable region.

4.2. Case II

In the second case, we assume the normalized mass flow rate, f_{in}, and the temperature shown in Fig. 9 and the system states have been initialized as $x_1(0) = 0.3253\,\mathrm{kg/m^3}$, $x_2(0) = 6363.7\,\mathrm{kg/m^3}$. Unlike Case I, in this second scenario the system is in an observable state from the outset. The observer parameters are exactly the same ones as in the previous section while the observer states have been initialized as $\hat{x}_1(0) = 1\,\mathrm{kg/m^3}$, $\hat{x}_2(0) = 6400\,\mathrm{kg/m^3}$.

The results of the simulation are illustrated in Fig. 10. Similarly to the previous case, the sorption rate estimator and $\hat{x}_1$ converge fast at the beginning. It can be noticed that $\hat{x}_2$ converges at the beginning but gradually deviates from the true value at $[2000, 4000)$s since this region is non-observable and $s_{fr} = 0$. Then $\hat{x}_2$ converges fast at $[4000, 6000)$s, gradually deviates from the true value at $[6000, 8000)$s and then converges fast again after 8000s.

The result of SOC estimation is shown in Fig. 11.

From the above two numerical simulations, it can be noticed that after the estimation of SOC converges, the discrepancy between the estimated value and the true value is almost not significant, even if it enters the non-observable region again, which shows the validation of the proposed SOC estimation architecture.

Table 3
Characteristics of the main sensors

Sensor	Model	Measure range
Mass flow meter	F-111B	0.16 mLn/min-25 Ln/min
Pressure sensor	PR-21Y	2 bar-30 bar
Thermocouple	K	−75 °C-260 °C

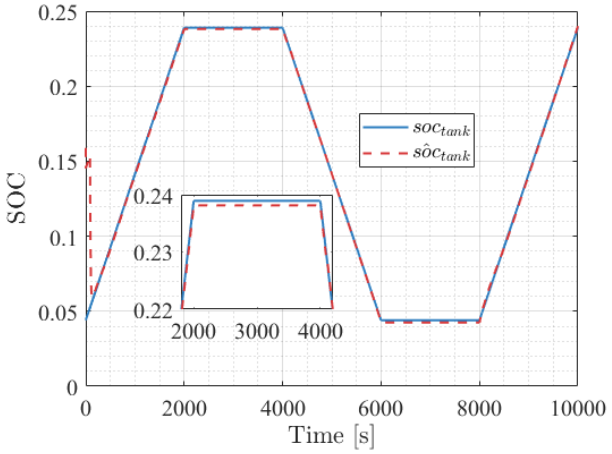

Fig. 11- Comparison of SOC estimation with true values for the simulation in Case II.

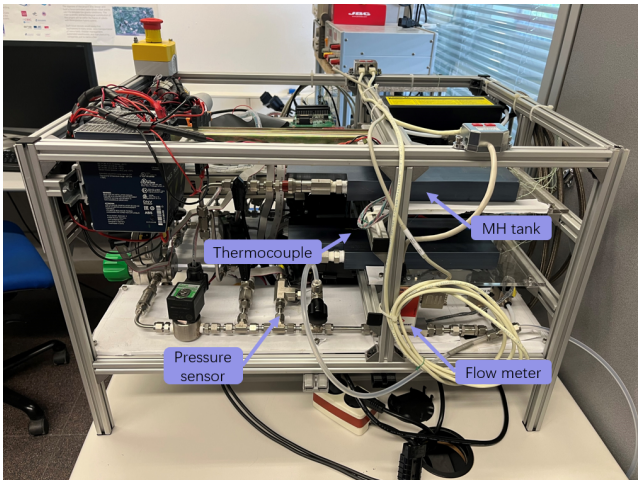

Fig. 12- View of the MH tank test bench environment.

5. Experimental validation

The proposed SOC estimation architecture has been validated in a practical MH tank test bench (Fig.12). The MH tank test bench consists of one MH tank (H2planet® MyH2 SLIM 350), hydrogen pipelines and sensors. The material for the tank is Hydralloy C5 ($Ti_{0.95}Zr_{0.05}Mn_{1.48}Fe_{0.08}Al_{0.01}$) and the MH tank is placed in the air for natural cooling.

Since the tank does not present homogeneous temperatures and the model uses a single temperature, which represents the average temperature, four thermocouples were incorporated, placed at different positions on the tank surface. The arithmetic mean of these measurements provides a representative measure of the tank's temperature; this mean is used to supply the tank.

Additionally, flow and pressure measurements are available from a flow sensor and a pressure gauge.

All signals are sampled at a constant sampling rate of 1s. All these elements are connected to a NI CompactRIO

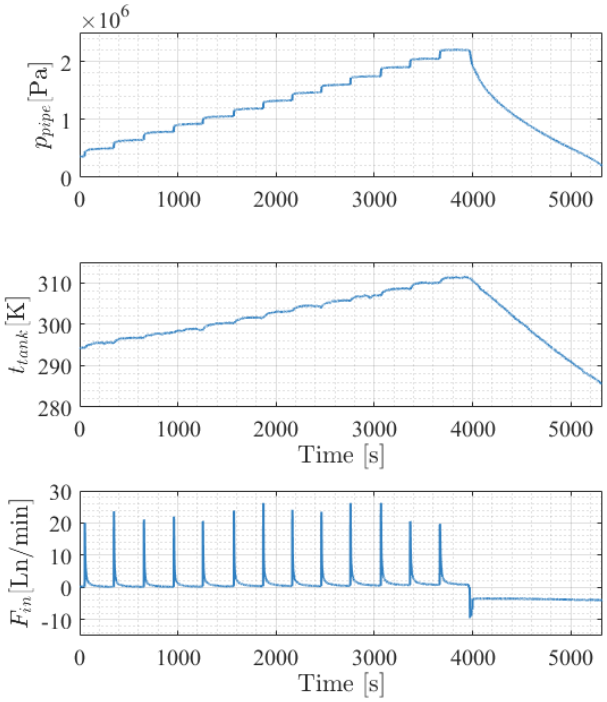

Fig. 13- Experiment measurable variables: pipe pressure p_{pipe}, tank temperature t_{tank} and flow rate F_{in}.

device responsible for storing and processing all the data. Table 3 lists the characteristics of the main sensors.

In a previous work [40], this same environment was used to characterize and adjust the hydride tank model used in this paper. It's worth noting that the range of the tank temperature and the mass flow rate are both close to the different practical temperature and mass flow rate ranges in the literature [24, 25].

Fig. 13 shows the evolution of measurable variables during the experiment: pipe pressure p_{pipe}, tank temperature t_{tank} and flow rate F_{in}. The system input, the tank pressure p, can be calculated using the pipe model as $p = p_{pipe} - f_{in}/k_p/10^{-5}$ where k_p is proportional coefficient and $f_{in} = \frac{M_{H_2} \cdot F_{in}}{v_{MH} \cdot 60 \cdot 22.4}$ [40].

The experiment is divided into two processes: charge and discharge. During the charge phase, the pressure of hydrogen released from the high-pressure tank is controlled by adjusting the pressure regulator and paying attention to the temperature of the tank so that it does not exceed the maximum operating temperature of the tank. In the discharge phase, the valve of the charge pipeline is closed while the valve of the discharge pipeline is opened to keep the flow rate steady. Before designing the observer, the model is calibrated using the method proposed in [40]. All the parameters are listed in Table 1.

During the implementation of the algorithm and its real-time execution, some problems have appeared. The main problem has been the calculation of $\bar{x}_2$. As already observed in our previous work [40], (35) has a problem fitting the experimental data. This is especially relevant during sudden

changes in flow. In those cases where (35) does not fit the data, its inverse, (16), does not have physical sense. The use of this data in the observer causes its performance to decrease significantly in transient behaviour. To avoid these problems, when the calculation of $\bar{x}_2$ is not considered correct its value is not used in the observer (i.e. it is assumed that $s_{fr} = 0$). This is detected either because the numerical solver does not find a solution, or because the solution obtained is not physically consistent (i.e. a positive $\hat{f}_r$ generates a decrease in $\bar{x}_2$).

The numerical resolution of the equation is time-consuming and cannot always be performed in real-time. The expression of f_r contains transcendental functions, (38) and (39), so obtaining explicit solutions for ψ_1 and ψ_2 is not possible. One approach that has been considered is the approximation of the inverse function by a neural network. This approach allows obtaining practically identical results but significantly reducing the computation time required. The input of the neural network is $(\bar{x}_1, u_1, \hat{f}_r)$ and the output is $\bar{x}_2$. The set of points required for neural network training is obtained by the grid technique. The ranges of neural network training inputs are set as $x_1 \in [0.1, 2][\mathrm{kg/m^3}]$, $x_2 \in [6360, 6600]$ $[\mathrm{kg/m^3}]$ and $u_1 \in [275, 320]$ [K]. The grid steps are 0.5, 0.02 and 1, respectively. Then we can calculate the corresponding f_r based on (35) to train two neural networks separately, one for absorption and the other for desorption.

The training of the neural network has been implemented using MATLAB's neural network toolbox. A neuronal network with 20 neurons in a single hidden layer has been chosen. The sigmoid function has been selected as an activation function in every neuron. Finally, the network has been trained using the Bayesian regularization algorithm and the mean-square error as a performance function. The results obtained by numerical resolution and the use of the neural network are shown in the last figure of Fig .15, for the experiment analyzed. As can be seen, the difference between both options is very small with errors that are negligible from a practical point of view.

The USDE time constant is fixed to $\kappa = 1$ to make it compatible with the sampling time and robust against measurement noise. The threshold to determine that the system is in a non-observable region is chosen as $\mu = 10^{-3}$. This value has been designed to know the sensor precision and the signal dynamic ranges. Finally, the observer gains have been fixed to $l_1 = 0.1$ and $l_2 = 0.1$ respectively. This selection offers a good trade-off between bandwidth (i.e. time constant) and the signal smoothness. The observer initial conditions are taken as $\hat{x}_1(0) = 1\,\mathrm{kg/m^3}$, $\hat{x}_2(0) = 6400\,\mathrm{kg/m^3}$.

The observer outputs, corresponding to the measurable variables shown in Fig. 13, are shown in Fig. 15. As can be seen, the proposed USDE converges almost immediately and offers a smooth estimation which tracks the evolution of f_{in}. It is important to emphasize that the true value of f_r cannot be directly measured. Fig. 15 shows the evolution of the estimation of ρ_g. The figure shows both $\bar{x}_1$ and $\hat{x}_1$, note that $\bar{x}_1$ corresponds to an algebraic estimation which is more sensitive to measurement noise while $\hat{x}_1$ offers a smoother estimation. Both estimations converge in steady-state. $\hat{x}_1$ converges after 50s.

Fig. 15 shows the evolution of $\hat{x}_2$ and $\bar{x}_2$. The figure shows the evolution of $\hat{x}_2$ and $\bar{x}_2$. As explained above, $\bar{x}_2$ is not always considered correct. Values considered correct are shown in green while those considered incorrect are shown in black, either because the system is in an unobservable zone or the numerical solver does not find a solution. When the estimate is correct, $\hat{x}_2$ converges towards $\bar{x}_2$, while when the estimate is incorrect, $\hat{x}_2$ evolves only taking into account the value of $\hat{f}_r$. The convergence of x_2 takes longer than that of x_1, around 400s. This is because, during this time interval, the system is in non-observable regions for a significant amount of time. From then on, the two estimates evolve quite similarly. A significant discrepancy occurs at the moment when the discharge starts, which produces a sudden change in the flow, which makes $\bar{x}_2$ not correct for a significant amount of time.

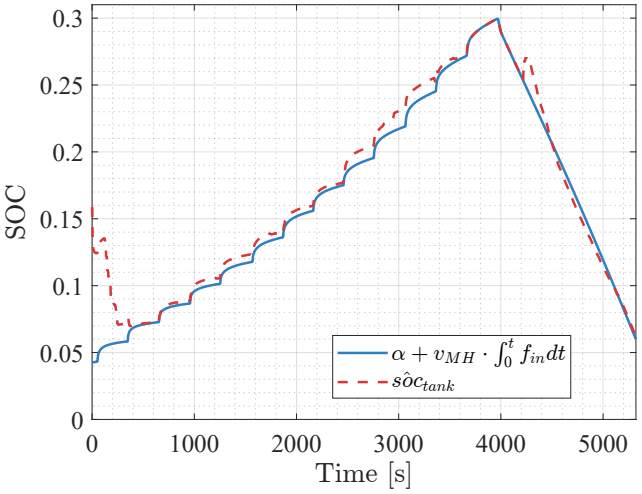

Fig. 14- SOC estimation: Comparison between the estimation framework (7) and an offline estimation.

Finally, Fig. 14 shows the evolution of the SOC estimation, $\hat{soc}_{tank}$, computed from $\hat{x}_1$ and $\hat{x}_2$. Since it is an algebraic estimation, the convergence time depends on the convergence time of $\hat{x}_1$ and $\hat{x}_2$ previously discussed. Since the exact value is not available, as it cannot be measured, (6) has been used to obtain an approximation. It should be noted that since the initial soc_{tank}, $m_{H_2}(0)$, is unknown, a posteriori value, α, has been calculated so that both curves are as close as possible. It is important to emphasize that this positioning can only be done offline once all the data is available. As can be seen, both curves follow a similar evolution. It can therefore be verified that the estimation of the SOC is quite reasonable based on the available information.

This section has allowed us to verify that the proposed observation architecture can be applied, with good results, to estimate the state of charge of the MH tank in real-time.

6. Conclusions

In this work, a simple and innovative architectural proposal has been made for estimating the state of charge of metal hydride tanks. The proposal combines the use of a simple tank model and easily obtained experimental data. Unlike other works in the literature, the proposal allows estimating the state of charge in dynamic situations and in real time.

The highlights of the paper are:

- The observability of the model used has been characterized. Based on this analysis, it has been determined under which conditions it is possible to estimate the state of charge and under which it is not.
- It has been demonstrated that once the tank has remained in an observable configuration for a sufficient amount of time, the proposed algorithm is capable of accurately estimating its state of charge. The experimental results show that the MH density (ρ_s), and therefore the state of charge of the MH tank, can be estimated in less than 400s.
- An estimator based on USDE has been designed, capable of estimating in real time, from the measured variables, the sorption rate of the MH tanks.
- An implementation based on neural networks has been proposed, which significantly reduces the computational burden required to implement the proposed algorithm. This significantly facilitates its implementation in industrial equipment.

The proposed algorithm has been validated both by numerical simulation and experimentally in commercial MH tanks.

One of the weaknesses of the algorithm is the need to invert the sorption mass flow function that describes the sorption flux. The function used is not able to correctly describe certain dynamic behaviors, which reduces the performance of the observer. Therefore, future work will focus on finding other mathematical expressions for the sorption mass flow function that are easily adjustable and better adapted during transient behaviors. The incorporation of the dynamic temperature model into the model used in the observer will also be addressed. This is expected to reduce the size of the unobservable regions.

Acknowledgement

This work is part of the Project MAFALDA (PID2021-126001OB-C31 funded by MCIN/ AEI /10.13039/501100011033 and by "ERDF A way of making Europe") and Project MASHED (TED2021-129927B-I00 funded by MCIN/AEI /10.13039/501100011033 and by the "European Union Next GenerationEU/PRTR").

This work is partially supported by National Natural Science Foundation of China under grant (62273169) and the Chinese Scholarship Council (CSC) under grant (202208530009).

A. Modeling of MH tanks

A.1. Mass balance

For hydrogen, the balance of mass is given by

$$\frac{\mathrm{d}\rho_{\mathrm{g}}}{\mathrm{dt}} = \frac{m'_{in} - m'_r}{v_{tank} - v_{MH} \cdot (1-\varepsilon)}, \tag{31}$$

where ρ_g is the density of hydrogen, m'_{in} is the mass of hydrogen entering or leaving the tank by unit time, m'_r is the mass of absorption or desorption of hydrogen by unit time, v_{tank} and v_{MH} are the volume of the tank and the MH (under the stacking state), respectively, and ε is the porosity of the MH. Therefore, the numerator of the right term of the above equation represents the change in mass of hydrogen per unit of time and the denominator represents the full volume of hydrogen inside the tank.

Define the normalized mass flow rate of hydrogen $f_{in} \triangleq m'_{in}/v_{MH}$, the normalized sorption mass flow rate of hydrogen $f_r \triangleq m'_r/v_{MH}$, the normalized volume of hydrogen $v_g \triangleq v_{tank}/v_{MH} - 1 + \varepsilon$. Then, (31) can be simplified to

$$\frac{\mathrm{d}\rho_{\mathrm{g}}}{\mathrm{dt}} = \frac{f_{in} - f_r}{v_g}. \tag{32}$$

Similarly, for the MH, one has

$$\frac{\mathrm{d}\rho_{\mathrm{s}}}{\mathrm{dt}} = \frac{m'_r}{v_{MH} \cdot (1-\varepsilon)}, \tag{33}$$

where ρ_s is the density of the MH and the denominator of the right term represents the full volume of the MH inside the tank. If one defines the normalized volume of the MH $v_s \triangleq 1 - \varepsilon$, then (33) can be simplified to

$$\frac{\mathrm{d}\rho_{\mathrm{s}}}{\mathrm{dt}} = \frac{f_r}{v_s}. \tag{34}$$

A.2. Reaction kinetics

The normalized sorption mass flow rate of hydrogen f_r can not be measured directly. A widely used model [45] is

$$f_r = \begin{cases} c_a e^{-\frac{E_a}{R \cdot t_{tank}}} \ln\left(\frac{p}{p_{eq,a}}\right)(\rho_{ss} - \rho_s),\ p > p_{eq,a}, & \text{(35a)} \\ c_d e^{-\frac{E_d}{R \cdot t_{tank}}} \left(\frac{p - p_{eq,d}}{p_{eq,d}}\right)(\rho_s - \rho_{s0}),\ p < p_{eq,d}, & \text{(35b)} \\ 0, \text{ otherwise.} & \text{(35c)} \end{cases}$$

where c_a and c_d are the absorption and desorption constants, E_a and E_d are the activation energy for absorption and desorption, R is universal gas constant, t_{tank} is the temperature of the MH tank, p is the MH tank pressure, and $p_{eq,a}$ and $p_{eq,d}$ are the equilibrium pressure for absorption and desorption, respectively. The terms $c_a e^{-E_a/Rt_{tank}}$ and $c_d e^{-E_d/Rt_{tank}}$ are rate coefficients obtained through the Arrhenius relationship [46]. ρ_{ss} is the density of the MH when the absorbed hydrogen reaches its maximum capacity, i.e. saturated density and ρ_{s0} is the density of the metal alloy (with no hydrogen).

The pressure, p, is assumed to obey the ideal gas equation of state:

$$p = \rho_g \frac{t_{tank} R}{M_{H_2}}. \tag{36}$$

where M_{H_2} is the molar mass of hydrogen.

The saturated density ρ_{ss} can be calculated by

$$\rho_{ss} = \rho_{s0} + \frac{\upsilon_{H_2} \cdot \rho_{H_2}}{\upsilon_{MH} \cdot (1-\epsilon)} \tag{37}$$

where υ_{H_2} is the capacity of hydrogen that can be absorbed by the tank, and ρ_{H_2} is the density of hydrogen (1 atm, 0 °C), which is considered a constant.

A.3. Equilibrium pressure

Van't Hoff equation describes the equilibrium constant of a reaction at different temperatures. Gonzatti et al. [47] used a modified Van't Hoff equation to calculate the value of equilibrium pressure:

$$p_{eq,a} = p_0 \cdot e^{\left(\frac{\Delta S_d}{R} - \frac{\Delta H_d}{R \cdot t_{tank}} + (\varphi+\varphi_0)\tan\left[\pi\left(\frac{\rho_s - \rho_{s0}}{\rho_{ss} - \rho_{s0}} - 0.5\right)\right] + \frac{\beta}{2}\right)}, \tag{38}$$

$$p_{eq,d} = p_0 \cdot e^{\left(\frac{\Delta S_d}{R} - \frac{\Delta H_d}{R \cdot t_{tank}} + (\varphi-\varphi_0)\tan\left[\pi\left(\frac{\rho_s - \rho_{s0}}{\rho_{ss} - \rho_{s0}} - 0.5\right)\right] - \frac{\beta}{2}\right)}. \tag{39}$$

where p_0 is the atmospheric pressure, ΔH_d and ΔS_d are the enthalpy change and the entropy change for desorption, respectively. φ and φ_0 are the plateau flatness coefficients, β is the plateau hysteresis coefficient.

B. Proof of Lemma 1

The derivative of $\mathcal{M}_{x_1}$ can be calculated as

$$\begin{aligned}\dot{\mathcal{M}}_{x_1} &= \frac{1}{\kappa} \cdot \left[\upsilon_g \dot{\bar{x}}_1 - \upsilon_g \cdot \frac{\bar{x}_1 - x_{1f}}{\kappa} + \kappa \dot{f}_r - \left(u_2 - u_{2f}\right) \right] \\ &= \frac{1}{\kappa} \cdot \left[-f_r - \left(\mathcal{M}_{x_1} - f_r\right) + \kappa \dot{f}_r \right] \\ &= -\frac{1}{\kappa} \cdot \left(\mathcal{M}_{x_1} - \kappa \dot{f}_r\right).\end{aligned} \tag{40}$$

To verify the boundedness of $\mathcal{M}_{x_1}$, the Lyapunov function $V_{\mathcal{M}} = \mathcal{M}_{x_1}^2/2$ is selected, with derivative

$$\begin{aligned}\dot{V}_{\mathcal{M}} &= -\frac{1}{\kappa}\mathcal{M}_{x_1}^2 + \mathcal{M}_{x_1}\dot{f}_r \\ &\le -\frac{1}{\kappa}\mathcal{M}_{x_1}^2 + \frac{1}{2\kappa}\mathcal{M}_{x_1}^2 + \frac{\kappa}{2}\dot{f}_r^2 \le -\frac{1}{\kappa}V_{\mathcal{M}} + \frac{\kappa}{2}\lambda^2.\end{aligned} \tag{41}$$

The solution of (41) satisfies $V_{\mathcal{M}}(t) \le e^{-t/\kappa}V_{\mathcal{M}}(0) + \kappa^2\lambda^2/2$. Then the following bound of the manifold variable can be obtained

$$|\mathcal{M}_{x_1}(t)| = \sqrt{2V_{\mathcal{M}}(t)} \le \sqrt{\mathcal{M}_{x_1}^2(0)e^{-t/\kappa} + \kappa^2\lambda^2}, \tag{42}$$

which means that $\mathcal{M}_{x_1}(t)$ will exponentially converge to $\kappa\lambda$ as time goes to infinity, i.e. $\lim_{t\to\infty}\mathcal{M}_{x_1} = \kappa\lambda$. In addition, for a sufficiently small filter parameter $\kappa \to 0$, $\mathcal{M}_{x_1}(t) \to 0$. Therefore, there exists an invariant manifold $\mathcal{M}_{x_1} = 0$ such that

$$\lim_{\kappa\to 0}\left[\lim_{t\to\infty}\mathcal{M}_{x_1}\right] = 0. \tag{43}$$

C. Proof of Theorem 2

Applying the low-pass filter operation to both sides of subsystem (17), we can obtain

$$\frac{s\bar{x}_1}{\kappa s+1} = \frac{1}{\upsilon_g} \cdot \left(\frac{u_2}{\kappa s+1} - \frac{f_r}{\kappa s+1}\right). \tag{44}$$

Then, similar to (20), we define the filtered version of f_r:

$$\kappa\dot{f}_{rf} + f_{rf} = f_r,\ f_{rf}(0) = 0, \tag{45}$$

so (44) can be written as

$$f_{rf} = u_{2f} - \upsilon_g \dot{x}_{1f} = u_{2f} - \upsilon_g \cdot \frac{\bar{x}_1 - x_{1f}}{\kappa}. \tag{46}$$

It is obvious that $\hat{f}_r = f_{rf}$ from (23) and (46). Now we consider the dynamic of $\tilde{f}_r$.

$$\dot{\tilde{f}}_r = \dot{f}_r - \dot{\hat{f}}_r = \dot{f}_r - \frac{f_r - f_{rf}}{\kappa} = -\frac{\tilde{f}_r}{\kappa} + \dot{f}_r. \tag{47}$$

Selecting the Lyapunov function $V_{f_r} = f_r^2/2$ one has

$$\dot{V}_{f_r} = -\frac{\tilde{f}_r^2}{\kappa} + \tilde{f}_r\dot{f}_r \le -\frac{1}{\kappa}V_{f_r} + \frac{\kappa}{2}\lambda^2. \tag{48}$$

The solution of (48) satisfies $V_{f_r}(t) \le e^{-t/\kappa}V_{f_r}(0) + \kappa^2\lambda^2/2$. Then the bound of the estimation error $\tilde{f}_r$ is

$$|\tilde{f}_r(t)| = \sqrt{2V_{f_r}(t)} \le \sqrt{\tilde{f}_r^2(0)e^{-t/\kappa} + \kappa^2\lambda^2}, \tag{49}$$

which means that $\tilde{f}_r(t)$ will exponentially converge to $\kappa\lambda$ as time goes to infinity, i.e. $\lim_{t\to\infty}\tilde{f}_r = \kappa\lambda$.

D. Proof of Theorem 3

Dynamics of observer error $\tilde{x}_1$ can be obtained by (17) and (24) as

$$\begin{aligned}\dot{\tilde{x}}_1 &= \frac{u_2 - f_r}{\upsilon_g} - \frac{u_2 - \hat{f}_r}{\upsilon_g} - l_1\tilde{x}_1 \\ &= -l_1\tilde{x}_1 - \frac{1}{\upsilon_g} \cdot (f_r - \hat{f}_r) = -l_1\tilde{x}_1 + \delta_1,\end{aligned} \tag{50}$$

where we define $\delta_1(t) \triangleq -(f_r - \hat{f}_r)/\upsilon_g$. Based on the result of the above section, $\lim_{t\to\infty}\delta_1(t) = -\kappa\lambda/\upsilon_g$.

We select the Lyapunov function $V_{\tilde{x}_1} = \tilde{x}_1^2/2$, and its derivative along (24) can be calculated as

$$\begin{aligned}\dot{V}_{\tilde{x}_1} &= -l_1\tilde{x}_1^2 + \delta_1\tilde{x}_1 \\ &\le -l_1\tilde{x}_1^2 + \frac{\tilde{x}_1^2}{2 \cdot \frac{1}{l_1}} + \frac{\frac{1}{l_1} \cdot \delta_1^2}{2} \\ &= -l_1 V_{\tilde{x}_1} + \frac{\delta_1^2}{2l_1}.\end{aligned} \tag{51}$$

The solution of (51) satisfies $V_{\tilde{x}_1}(t) \leq e^{-l_1 t} V_{\tilde{x}_1}(0) + \delta_1^2/(2l_1)$, which implies

$$|\tilde{x}_1(t)| = \sqrt{2V_{\tilde{x}_1}(t)} \leq \sqrt{\tilde{x}_1^2(0)e^{-l_1 t} + \delta_1^2/{l_1}^2}. \quad (52)$$

Thus, $\tilde{x}_1(t)$ will exponentially converge to $\kappa\lambda/(l_1 v_g)$ as time goes to infinity, i.e. $\lim_{t\to\infty} \tilde{x}_1(t) = \kappa\lambda/(l_1 v_g)$. To make the error $\tilde{x}_1$ small enough, observer gain l_1 should be chosen large enough.

E. Proof of Theorem 4

The evolution of $\tilde{x}_2$, (29), can be bounded as

$$\begin{aligned}
|\tilde{x}_2(t)| &= \left|\phi(t)\cdot\tilde{x}_2(0) + \phi(t)\cdot\int_0^t \frac{\tilde{f}_r(\tau)}{v_s}\phi(\tau)d\tau\right| \\
&\leq |\phi(t)\cdot\tilde{x}_2(0)| + \left|\phi(t)\cdot\int_0^t \frac{\tilde{f}_r(\tau)}{v_s}\phi(\tau)d\tau\right| \\
&\leq \phi(t)|\tilde{x}_2(0)| + \frac{\|\tilde{f}_r\|_\infty}{v_s}\left|\phi(t)\cdot\int_0^t \phi(\tau)d\tau\right| \\
&= \phi(t)|\tilde{x}_2(0)| + \frac{\|\tilde{f}_r\|_\infty}{v_s}\left|e^{-l_2\varpi t}\cdot\frac{1}{l_2\varpi}\cdot e^{l_2\varpi\tau}\Big|_0^t\right| \\
&= e^{-l_2\varpi t}|\tilde{x}_2(0)| + \frac{\|\tilde{f}_r\|_\infty}{v_s}\frac{1-e^{-l_2\varpi t}}{l_2\varpi},
\end{aligned}$$

Thus, $\tilde{x}_2(t)$ will exponentially converge to a ball of radius $\|\tilde{f}_r\|_\infty/(v_s\cdot l_2\cdot\varpi)$, i.e.

$$\lim_{t\to\infty}|\tilde{x}_2| < \frac{\|\tilde{f}_r\|_\infty}{(v_s\cdot l_2\cdot\varpi)}.$$

References

[1] R. Moliner-Heredia, C. Vivas, F. R. Rubio, Optimal management in microgrids with photovoltaic and green hydrogen support., Revista Iberoamericana de Automática e Informática industrial (2024).

[2] D. Tang, G.-L. Tan, G.-W. Li, J.-G. Liang, S. M. Ahmad, A. Bahadur, M. Humayun, H. Ullah, A. Khan, M. Bououdina, State-of-the-art hydrogen generation techniques and storage methods: A critical review, Journal of Energy Storage 64 (2023) 107196.

[3] A. L. M. Reddy, A. E. Tanur, G. C. Walker, Synthesis and hydrogen storage properties of different types of boron nitride nanostructures, international journal of hydrogen energy 35 (2010) 4138–4143.

[4] M. R. Usman, Hydrogen storage methods: Review and current status, Renewable and Sustainable Energy Reviews 167 (2022) 112743.

[5] P. Preuster, A. Alekseev, P. Wasserscheid, Hydrogen storage technologies for future energy systems, Annual review of chemical and biomolecular engineering 8 (2017) 445–471.

[6] F. Zhang, P. Zhao, M. Niu, J. Maddy, The survey of key technologies in hydrogen energy storage, International journal of hydrogen energy 41 (2016) 14535–14552.

[7] M. Afzal, R. Mane, P. Sharma, Heat transfer techniques in metal hydride hydrogen storage: A review, International Journal of Hydrogen Energy 42 (2017) 30661–30682.

[8] J. Tarascon, M. Armand, Materials for sustainable energy: a collection of peer-reviewed research and review articles from nature publishing group, 2011.

[9] K. V. Krishna, V. Pandey, M. Maiya, Bio-inspired leaf-vein type fins for performance enhancement of metal hydride reactors, International Journal of Hydrogen Energy 47 (2022) 23694–23709.

[10] D. Wang, Y. Wang, Z. Huang, F. Yang, Z. Wu, L. Zheng, L. Wu, Z. Zhang, Design optimization and sensitivity analysis of the radiation mini-channel metal hydride reactor, Energy 173 (2019) 443–456.

[11] S. Zhang, F. Yang, L. Zhou, Y. Zhang, Z. Wu, Z. Zhang, Y. Wang, A novel multilayer fin structure for heat transfer enhancement in hydride-based hydrogen storage reactor, International Journal of Energy Research 42 (2018) 3837–3850.

[12] X.-S. Bai, W.-W. Yang, Y.-J. Yang, K.-R. Zhang, F.-S. Yang, Multivariable optimization of metal hydride hydrogen storage reactor with gradient porosity metal foam and evaluation of comprehensive performance, International Journal of Hydrogen Energy 47 (2022) 35340–35351.

[13] A. Chibani, S. Merouani, C. Bougriou, A. Dehane, Heat and mass transfer characteristics of charging in a metal hydride-phase change material reactor with nano oxide additives: the large scale-approach, Applied Thermal Engineering 213 (2022) 118622.

[14] A. Chibani, S. Merouani, N. Gherraf, I. Ferhoune, Y. Benguerba, Numerical investigation of heat and mass transfer during hydrogen desorption in a large-scale metal hydride reactor coupled to a phase change material with nano-oxide additives, International Journal of Hydrogen Energy 47 (2022) 14611–14627.

[15] J. Xiao, L. Tong, T. Yang, P. Bénard, R. Chahine, Lumped parameter simulation of hydrogen storage and purification systems using metal hydrides, International Journal of Hydrogen Energy 42 (2017) 3698–3707.

[16] M. Raju, J. P. Ortmann, S. Kumar, System simulation model for high-pressure metal hydride hydrogen storage systems, International Journal of Hydrogen Energy 35 (2010) 8742–8754.

[17] A. Fopah-Lele, A. Kabore-Kere, J. G. Tamba, I. Yaya-Nadjo, Solar electricity storage through green hydrogen production: A case study, International Journal of Energy Research 45 (2021) 13007–13021.

[18] G. Jansen, Z. Dehouche, H. Corrigan, Cost-effective sizing of a hybrid regenerative hydrogen fuel cell energy storage system for remote & off-grid telecom towers, International Journal of Hydrogen Energy 46 (2021) 18153–18166.

[19] H. Q. Nguyen, B. Shabani, Thermal management of metal hydride hydrogen storage using phase change materials for standalone solar hydrogen systems: An energy/exergy investigation, International Journal of Hydrogen Energy 47 (2022) 1735–1751.

[20] J. Liu, F. Yang, Z. Wu, Z. Zhang, A hybrid modeling method of metal hydride tank and dynamic characteristic analysis, International Journal of Hydrogen Energy 50 (2024) 799–811.

[21] J. Liu, J. Wang, F. Yang, Z. Wu, Z. Zhang, The analysis of cross-level transfer characteristic of hydrogen and heat of thermal coupling system: Framework design and case study, Energy (2025) 135899.

[22] F. Gonzatti, F. Farret, Mathematical and experimental basis to model energy storage systems composed of electrolyzer, metal hydrides and fuel cells, Energy Conversion and Management 132 (2017) 241–250.

[23] S. Suarez, D. Chabane, A. N'Diaye, Y. Ait-Amirat, A. Djerdir, Static and dynamic characterization of metal hydride tanks for energy management applications, Renewable Energy 191 (2022) 59–70.

[24] D. Zhu, D. Chabane, Y. Ait-Amirat, A. N'Diaye, A. Djerdir, Estimation of the state of charge of a hydride hydrogen tank for vehicle applications, in: 2017 IEEE Vehicle Power and Propulsion Conference (VPPC), IEEE, 2017, pp. 1–6.

[25] D. Zhu, Y. Ait-Amirat, A. N'Diaye, A. Djerdir, On-line state of charge estimation of embedded metal hydride hydrogen storage tank based on state classification, Journal of Energy Storage 42 (2021) 102950.

[26] T. Puleston, A. Cecilia, R. Costa-Castelló, M. Serra, Nonlinear observer for online concentration estimation in vanadium flow batteries based on half-cell voltage measurements, Computers & Chemical Engineering 185 (2024) 108664.

[27] A. Cecilia, D. Astolfi, R. Costa-Castelló, A new nonlinear observer for liquid water estimation in fuel cells, IEEE Transactions on Control Systems Technology 32 (2024) 990–1001.

[28] X. Wang, H. Su, F. Zhang, G. Chen, A robust distributed interval observer for lti systems, IEEE Transactions on Automatic Control 68 (2023) 1337–1352.

[29] X. Wang, Z. Fan, L. Wang, H. Su, J. Lam, Fully distributed observer design for mobile targets, IEEE Transactions on Network Science and Engineering 10 (2023) 1696–1708.

[30] X. Wang, W. Xu, H. Su, Z. Gao, G. Chen, Designing a completely distributed interval observer for the lti system, IEEE Transactions on Automatic Control (2024).
[31] G. Ciccarella, M. Dalla Mora, A. Germani, A luenberger-like observer for nonlinear systems, International Journal of Control 57 (1993) 537–556.
[32] G. Besançon, G. Bornard, H. Hammouri, Observer synthesis for a class of nonlinear control systems, European Journal of control 2 (1996) 176–192.
[33] J.-P. Gauthier, H. Hammouri, S. Othman, A simple observer for nonlinear systems applications to bioreactors, IEEE Transactions on automatic control 37 (1992) 875–880.
[34] D. Astolfi, L. Marconi, L. Praly, A. R. Teel, Low-power peaking-free high-gain observers, Automatica 98 (2018) 169–179.
[35] P. Bernard, Observer design for nonlinear systems, volume 479, Springer, 2019.
[36] A. L. J. Keow, A. Mayhall, M. Cescon, Z. Chen, Active disturbance rejection control of metal hydride hydrogen storage, International Journal of Hydrogen Energy 46 (2021) 837–851.
[37] Q. Li, X. Lin, Q. Luo, Y. Chen, J. Wang, B. Jiang, F. Pan, Kinetics of the hydrogen absorption and desorption processes of hydrogen storage alloys: A review, International Journal of Minerals, Metallurgy and Materials 29 (2022) 32–48.
[38] G. Sandrock, A panoramic overview of hydrogen storage alloys from a gas reaction point of view, Journal of alloys and compounds 293 (1999) 877–888.
[39] J.-H. Cho, S.-S. Yu, M.-Y. Kim, S.-G. Kang, Y.-D. Lee, K.-Y. Ahn, H.-J. Ji, Dynamic modeling and simulation of hydrogen supply capacity from a metal hydride tank, International journal of hydrogen energy 38 (2013) 8813–8828.
[40] M. Chen, C. Batlle, B. Escachx, R. Costa-Castelló, J. Na, Sensitivity analysis and calibration for a two-dimensional state-space model of metal hydride storage tanks based on experimental data, Journal of Energy Storage 94 (2024) 112316.
[41] G. Besançon, Nonlinear observers and applications, volume 363, Springer, 2007.
[42] P. Bernard, V. Andrieu, D. Astolfi, Observer design for continuous-time dynamical systems, Annual Reviews in Control 53 (2022) 224–248.
[43] R. Hermann, A. Krener, Nonlinear controllability and observability, IEEE Transactions on automatic control 22 (1977) 728–740.
[44] J. Na, B. Jing, Y. Huang, G. Gao, C. Zhang, Unknown system dynamics estimator for motion control of nonlinear robotic systems, IEEE Transactions on Industrial Electronics 67 (2019) 3850–3859.
[45] B. D. MacDonald, A. M. Rowe, Impacts of external heat transfer enhancements on metal hydride storage tanks, International Journal of Hydrogen Energy 31 (2006) 1721–1731.
[46] D. A. Nield, A. Bejan, et al., Convection in porous media, volume 3, Springer, 2006.
[47] F. Gonzatti, M. Miotto, F. Farret, Automation and analysis of the operation of (la0. 85ce0. 15) ni5 in energy storage plants, international journal of hydrogen energy 43 (2018) 2850–2860.

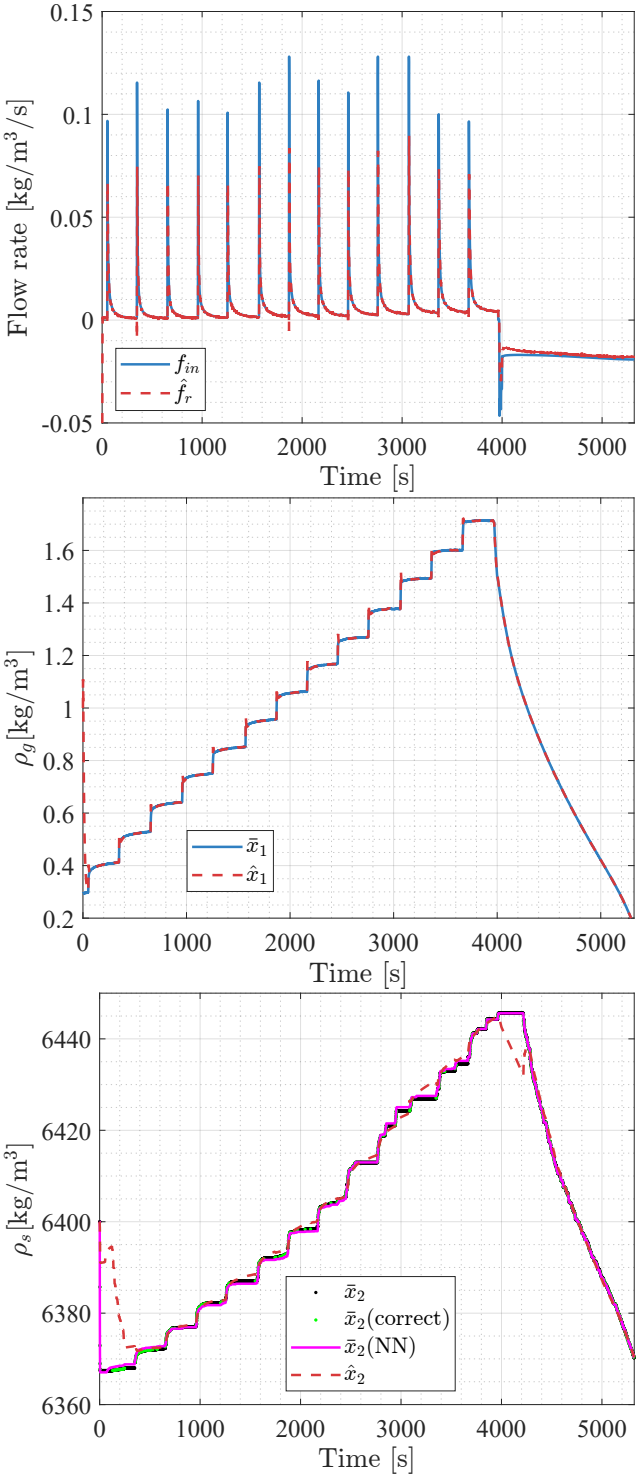

Fig. 15- Observer results obtained for the experimental results. Top: Comparison between the estimation (23) and normalized mass flow rate f_{in}; Middle: Comparison between the observer (24) and the calculated value $\bar{x}_1$; Bottom: Comparison between the observer (26) and inverted value $\bar{x}_2$.